Title

Inversion of Many-Beam Bragg Intensities for Phasing by Iterated Projections: Removal of Multiple Scattering Artifacts from Diffraction Data

Journal

Physical Review Letters, 125(6)

ISSN

0031-9007

Authors

Donatelli, Jeffrey J

Spence, John CH

Publication Date

2020-08-07

DOI

10.1103/physrevlett.125.065502

Peer reviewed

Inversion of Many-Beam Bragg Intensities for Phasing by Iterated Projections: Removal of Multiple Scattering Artifacts from Diffraction Data

Jeffrey J. Donatelli[1,2] and John C. H. Spence[3]
[1]*Department of Applied Mathematics, Lawrence Berkeley National Laboratory, Berkeley, California 94720, USA*
[2]*Center for Advanced Mathematics for Energy Research Applications, Lawrence Berkeley National Laboratory, Berkeley, California 94720, USA*
[3]*Department of Physics, Arizona State University, Tempe, Arizona 85287-1504, USA*

An iterated projection algorithm (N-Phaser) is developed that reconstructs a scattering potential from N-beam multiple Bragg scattered intensities. The method may be used to eliminate multiple scattering artifacts from electron diffraction data, solving the phase problem and increasing the thicknesses of samples used in materials science, solid-state chemistry, and small molecule crystallography. For high-energy transmission electron diffraction, we show that the algorithm recovers accurate complex structure factors from a wide range of thicknesses, orientations, and relativistic beam energies, and does not require known thickness or atomic-resolution data if sufficient multiple scattering occurs. Extensions to Cryo-electron microscopy and Micro-electron diffraction are suggested.

Multiple elastic scattering in x-ray, electron, and neutron diffraction prevents extraction of structure factors, but is useful for standing waves (modulating fluorescence), chirality, and space-group determination, and for phase determination. The size limit which multiple scattering imposes on samples severely hampers the effort toward whole-cell imaging in cryoelectron microscopy, the size of protein microcrystals analyzed by the new method of Micro-electron diffraction, sample thickness in coherent x-ray diffractive imaging, and the thickness of the crystals and their defects (which control the properties of matter) which may be imaged by atomic-resolution transmission electron microscopy (TEM) in condensed matter physics and materials science.

Since interference between Bragg components of Bloch waves excited inside a crystal is the basis of the effect, multiply scattered Bragg intensities are sensitive to structure factor phases. Inversion from multiple to single scattering therefore solves the phase problem, by recovering complex structure factors. Three-beam cases may allow phasing for inorganic crystallography (see, e.g., Ref. [1]). The phase problem is an urgent issue in Micro-electron diffraction, where protein microcrystal structures are solved by transmission electron diffraction (TED) using Cryo-electron microscopy instrumentation with thousands of simultaneously excited Bragg beams. Direct methods are limited by the number of atoms in the molecule, while molecular replacement depends on existing models. With the development of nanometer-diameter x-ray beams, a general solution to this problem would also provide an x-ray microdiffraction technique giving phased lensless images of small regions of much thicker samples in materials science and biology.

Since Bethe's formulation [2] of the multiple electron scattering problem in explanation of the Davisson-Germer experiment, there have been several distinct alternative formulations, including multislice, Darwin equation, Bloch-wave, scattering matrix, and path integral approaches [3,4]. Partially successful inversion schemes for N-beam TED, which would recover the same complex structure factors $V_{\mathbf{g}}$ from measured Bragg intensities at any thickness, have been based on closed-form solutions [5,6], large-angle convergent-beam patterns [7], dynamical ptychography [8], optical multislice ptychography [9], iterated projections [10], data collected at two adjacent beam energies [11,12], and inversion from a scattering matrix S [13]. Although limited by lens resolution, inversion from the complex multiply scattered amplitudes which form atomic-resolution scanning transmission electron microscopy images [14], using multiple detector pixels to provide simultaneous tilted images, is an important recent advance.

The scattering matrix solution to a relativistically corrected Schroedinger equation, describing high-energy transmission electron diffraction (HEED) through a slab of crystal of thickness t, is defined as $S = \exp(2\pi i A t)$ [15]. Here the matrix A of order N contains entries $\sigma V_{\mathbf{g}}/(2\pi) = 1/(2\xi_{\mathbf{g}}) = U_{\mathbf{g}}/(2K)$ in off-diagonal positions, where the wanted structure factors $V_{\mathbf{g}}$ (in volts) or $U_{\mathbf{g}}$ (potential energy terms in Hamiltonian A) are the Fourier coefficients of the Coulomb potential $V(\mathbf{r})$. $\xi_{\mathbf{g}}$ is an extinction distance, $K \sim 1/\lambda'$ a corrected beam wave vector, and $\sigma = 2\pi m|e|\lambda/h^2$ with m the relativistic electron mass. The diagonal of A contains known excitation errors $s_{\mathbf{g}} = \lambda \mathbf{g}^2/2$ in symmetric zone axis orientations [for lattice vectors

$\mathbf{g} = \mathbf{g}(h,k,l)$] which define the diffraction conditions and kinetic energy (beam wavelength and direction). For example, for $N = 5$,

$$A = \frac{1}{2K}\begin{bmatrix} s_{\mathbf{h}} & U_{\mathbf{h}-\mathbf{g}} & U_{\mathbf{h}} & U_{\mathbf{h}+\mathbf{g}} & U_{2\mathbf{h}} \\ U_{\mathbf{g}-\mathbf{h}} & s_{\mathbf{g}} & U_{\mathbf{g}} & U_{2\mathbf{g}} & U_{\mathbf{g}+\mathbf{h}} \\ U_{-\mathbf{h}} & U_{-\mathbf{g}} & 0 & U_{\mathbf{g}} & U_{\mathbf{h}} \\ U_{-\mathbf{g}-\mathbf{h}} & U_{-2\mathbf{g}} & U_{-\mathbf{g}} & s_{-\mathbf{g}} & U_{-\mathbf{g}+\mathbf{h}} \\ U_{-2\mathbf{h}} & U_{-\mathbf{h}-\mathbf{g}} & U_{-\mathbf{h}} & U_{-\mathbf{h}+\mathbf{g}} & s_{-\mathbf{h}} \end{bmatrix}.$$

The moduli of the elements of S are proportional to the intensities of the transmitted Bragg beams. Each column of S contains magnitudes from one two-dimensional Bragg diffraction pattern, while adjacent columns correspond to patterns obtained by changing the incident beam direction to a succession of different Bragg conditions around the zone axis orientation [8]. As for crystal band structure, the HEED Bloch-wave solutions are periodic in the transverse component of K, lying in the first Brillioun zone, giving periodicity relations for both eigenvalues and eigenvectors of A [16]. In the absence of inelastic scattering, A is Hermitian, S is unitary and symmetric, and the problem amounts to inverting this unitary transformation, given the magnitudes of the entries in S (which we assume given), the diagonal of A, and its many symmetries. Symmetries are imposed by the space group of the crystal [17], an antidiagonal symmetry [13], and the fact that the same difference between indices on the diagonal (which defines off-diagonal element positions) occurs more than once. See Fig. S2 in Supplemental Material for an overview of the relation between the scattering potential and the scattering matrix magnitude data [18]. Inelastic scattering (absorption) destroys the orthogonality of A.

The first-order expansion of the exponential (single scattering, or first Born approximation) relates the three-dimensional crystallographic indices of entries in the two-dimensional matrix S to those of A. Since all of S is needed, inversion from one dynamical diffraction pattern in a single orientation is impossible [19].

In general, forward and reverse computation between A and S is possible. In particular, both matrices share the same eigenvectors, and the eigenvalues γ_i of A are related to the eigenvalues λ_i of S by $\lambda_i = \exp(2\pi i \gamma_i t)$. Therefore, $\gamma_i = \log(\lambda_i)/(2\pi i t) + n_i/t$, where n_i is an integer determined by the logarithm branch. The known diagonal of A provides N linear constraints which assist in solving for the N branch indices n_i, and thus for A. Remarkably, A can also be recovered without knowledge of the thickness t by solving for γ_i directly instead of the branch cuts. In some situations, such as for a symmetric zone axis orientation, these linear equations can become linearly independent, but additional linear constraints based on the known symmetries of A (see Ref. [13]) can be used to improve the invertibility of the linear system.

If the phases of S are measured, then the linear system described above provides direct one-step inversion from complex S to A [13]. This is the basis of the successful imaging method of Ref. [14]. Interferometric methods (such as ptychography and imaging) are, however, sensitive to instrumental phases (e.g., focusing errors, sample movement between tilts), which may then affect structure factor phase estimates. Instead, here we describe inversion from Bragg intensities, which is more robust, insensitive to sample displacement at the atomic scale, is not limited by the resolution of imaging lenses, and does not involve loss of relative phase information between tilts.

Use of the orthogonality constraint equations for S to find its complex entries from their magnitudes produces a system of nonlinear equations which are not readily solved except for small N. In fact, the number of orthogonal matrices whose elements have given magnitudes is very large [20]. In addition, for large thickness t, small changes in γ produce very large changes in λ, leading to instabilities in inversion.

In an earlier paper [10], we studied the nonconvex iteration between the set of all S matrices obtained from A with correct symmetry and diagonal, and the set of all S matrices with given magnitudes, providing successful phase retrieval at moderate thickness, but unstable at large. Our improved algorithm (N-Phaser) imposes these three constraints via iterative Bregman projections [21], while avoiding the instability at large thickness and, optionally, incorporating an additional "charge-flipping" step to assist phasing. Charge flipping (here potential flipping, demonstrated for experimental HEED in Ref. [22]) requires atomic-resolution data, and, by driving the potential to zero between atoms, applies an atomicity constraint [23]. Our resulting method recovers complex structure factors from Bragg TED intensities over a wide range of thickness, orientation, and beam energies.

Our goal is to reconstruct the real-space potential $V(\mathbf{r})$ from the scattering matrix magnitudes $M_{ij} = |S_{ij}|$. Initially we limit our treatment to recovering 2D projected potentials from HEED with all reciprocal lattice vectors lying in a plane normal to the beam (but with curved Ewald sphere), and discuss other cases below. A finite value of the zero-order structure factor (gauge transformation) appears as an unobservable phase factor on Bragg beams for a parallel-sided slab.

Computational trials suggest that three constraints are sufficient to define a "unique" solution: the symmetry constraints on A, its known diagonal, and the known magnitudes of the elements of S. By "unique" we refer to equivalent solutions differing by an origin shift on $V(\mathbf{r})$, which appears as a similarity transform on S, leaving eigenvalues unchanged. A reversal in the chirality (hand) of $V(\mathbf{r})$, as for the two forms of quartz, or the enantiomorphs important for small molecules in the drug industry, does affect the Bragg intensities under multiple scattering, but

not under single scattering, so these are not equivalent multiple scattering solutions, allowing enantiomorphs to be distinguished.

We now describe our algorithm for reconstructing the potential $V(\mathbf{r})$ from the scattering matrix magnitudes M. Initially we assume that the crystal thickness t is known. The algorithm begins with a random initial potential $V^0(\mathbf{r})$, and during the nth iteration performs the following operations (see Figs. S3–S6 in Supplemental Material for flow diagrams [18]).

(1) Compute the Fourier transform $V^n_{\mathbf{g}}$ from $V^n(\mathbf{r})$.

(2) Construct the structure matrix $A^n_{ii} = s_{\mathbf{g}_i}$, and for $i \neq j$, $A^n_{ij} = V^n_{\mathbf{g}_i - \mathbf{g}_j}$.

(3) Compute the eigenvalue expansion $A^n = U^n \Gamma^n U^{n*}$.

(4) Compute the matrix exponential via $S^n = U^n \Lambda^n U^{n*}$, where $\Lambda^n_{ii} = \exp(2\pi i \Gamma^n_{ii} t)$.

(5) Renormalize S^n to be consistent with the magnitude data via $\tilde{S}^n_{ij} = (S^n_{ij}/|S^n_{ij}|)M_{ij}$.

(6) Transform $\tilde{S}^n$ into a unitary matrix by computing the Schur decomposition $\tilde{S}^n = \tilde{U}^n T^n \tilde{U}^{n*}$, and then zero out the off-diagonal elements $\tilde{T}^n_{ij} = 0$ for $i \neq j$ and normalize the diagonal $\tilde{T}^n_{ii} = T^n_{ii}/|T^n_{ii}|$ [24].

(7) Update the structure matrix as $\tilde{A}^n = \tilde{U}^n \tilde{\Gamma}^n \tilde{U}^{n*}$, where $\tilde{\Gamma}^n_{ii} = \log(\tilde{T}^n_{ii})/(2\pi i t) + \eta_i/t$, the branch index is estimated as

$$\eta_i = \text{round}[x_i t - \log(\tilde{T}^n_{ii})/(2\pi i)],$$
$$x = y + D^{\dagger}(b - Dy), \qquad y_i = (\tilde{U}^{n*} A^n \tilde{U}^n)_{ii},$$

$D_{ij} = |U^n_{ij}|^2$, $b_i = s_{\mathbf{g}_i}$, and $D^{\dagger}$ is the pseudoinverse of D. When D is nonsingular, the y contributions cancel out in the above equation. However, when D is singular, the above equation will choose the solution that minimizes the structure matrix perturbation $||\tilde{A}^n - A^n||_F$.

(8) Average symmetry-related structure factors for $\mathbf{g} \neq \mathbf{0}$ from A via

$$\tilde{V}^n_{\mathbf{g}} = \begin{cases} \frac{1}{N_{\mathbf{g}}} \sum\limits_{(i,j)\in\mathbf{g}} A^n_{ij} & \text{if } N_{\mathbf{g}} \geq N_{\min} \\ 0 & \text{otherwise,} \end{cases}$$

where $(i,j) \in \mathbf{g}$ refers to the set of index pairs such that $\mathbf{g}_i - \mathbf{g}_j = \mathbf{g}$, and $N_{\mathbf{g}}$ is the number of such pairs. In particular, the structure factors that only have a few entries in A are set to 0 to improve stability of the algorithm. The constant component is allowed to float, i.e., $\tilde{V}^n_{\mathbf{0}} = V^n_{\mathbf{0}}$.

(9) Compute the inverse Fourier transform to get the potential $\tilde{V}^n(\mathbf{r})$.

(10) Update the potential via

$$V^{n+1}(\mathbf{r}) = \begin{cases} \tilde{V}^n(\mathbf{r}) & \text{if } \tilde{V}^n(\mathbf{r}) \geq \tau \\ \alpha \tilde{V}^n(\mathbf{r}) & \text{if } \tilde{V}^n(\mathbf{r}) < \tau, \end{cases}$$

where $0 < \alpha \leq -1$ corresponds to charge flipping, $\alpha = 0$ for flattening, and $\alpha = 1$ if neither flipping or flattening is used.

In the limiting case of small thickness, the above algorithm is equivalent to standard phasing using charge flipping alone. However, note that flipping requires the 2D projected potential to be sufficiently sparse, and so may not be effective in recovering 2D projections of very complex 3D crystal structures. If the thickness t is not precisely known, it can, depending on the physical parameters, be inferred during the reconstruction procedure. We accomplish this with a modification to step (4), where we use a golden section search to find the value of t that minimizes the Frobenious norm between the magnitudes of S^n and the magnitude data M.

Note that λ_i depends only on $\gamma_i - \lfloor \gamma_i t \rfloor / t$, which for large t becomes completely dominated by small perturbations to γ_i. Therefore, when the thickness becomes large, so that $\gamma_i t \gg 1$, calculation of λ from γ in step (4) becomes unstable. However, the eigenvectors of S can still be stably computed from A. To handle this instability for large t, we no longer compute the eigenvalues of S from A and instead use the magnitude constraint on S to estimate its eigenvalues. Hence, knowledge of the thickness is no longer needed in this case. Furthermore, in step (7), $\tilde{\Gamma}^n_{ii} \approx x_i$ when t is large, and so we modify this step to solve for $\tilde{\Gamma}_{ii}$ directly instead of determining the branch index. With these modifications, the algorithm no longer requires an estimate of the thickness. The modifications to steps (4) and (7) for the large thickness case are as follows.

(4b) The scattering matrix is computed as $S^n = U^n \Lambda^n U^{n*}$, where Λ^n is now given by the minimizer of

$$\Lambda^n = \text{argmin}_{\Lambda} \sum_{i,j} [|(U^n \Lambda U^{*n})_{ij}| - M_{ij}]^2.$$

Here we approximate this minimizer by using another iterative projection algorithm starting with $S = S^{n-1}$ and then applying several iterations of the following: (i) $S_{ij} = (S_{ij}/|S_{ij}|)M_{ij}$, (ii) $\Lambda_{ii} = (U^{n*} S U^n)_{ii}$, $\Lambda_{ij} = 0$ for $i \neq j$, (iii) $S = U^n \Lambda U^{n*}$.

(7b) Same as (7) except we take $\Gamma_{ii} = x_i$.

For the $n = 1$ iteration, we initialize S^0 to be a random unitary matrix. Since this second algorithm does not enforce the relationship between γ and λ, it may lead to an information deficiency for very small thickness, and is not equivalent to standard charge flipping alone.

The above two algorithms could be merged into one, in which case one would compute the eigenvalues λ_i of S from only the small eigenvalues γ_i of A and would instead use the magnitude constraint on S to determine the remaining λ_i. If not all columns of M can be measured, then reconstruction may still be possible by allowing the magnitudes of the missing columns to float during

TABLE I. Pearson correlation coefficients between the potentials of the reconstruction and ground truth for GaAs at three thicknesses and beam energies, using both versions of the algorithm for computing λ and flipping.

	λ from A, flipping			λ from M, flipping		
	10 nm	100 nm	1000 nm	10 nm	100 nm	1000 nm
100 kV	0.98	0.90	0.82	0.96	0.95	0.96
300 kV	0.97	0.89	0.80	0.90	0.97	0.96
1000 kV	0.97	0.84	0.57	0.82	0.70	0.67

TABLE II. Pearson correlation coefficients between the potentials of the reconstruction and ground truth for GaAs and spinel at three thicknesses and beam energies, by computing λ from M without flipping.

	GaAs, λ from M			Spinel, λ from M		
	10 nm	100 nm	1000 nm	10 nm	100 nm	1000 nm
100 kV	0.46	0.97	0.93	0.88	0.96	0.96
300 kV	0.29	0.97	0.96	0.93	0.98	0.97
1000 kV	0.97	0.74	0.77	0.5	0.98	0.95

reconstruction, i.e., by only performing the update in (5) where M_{ij} is available.

We applied the N-Phaser algorithms to scattering matrix magnitude data with $N = 441$ generated by a simulated tilt series of diffraction patterns from the GaAs noncentrosymmetric crystal structure with axial beam direction [110], and from a spinel crystal with beam direction [100]. We tested beam energies of 100, 300, and 1000 kV and crystal thicknesses 10, 100, and 1000 nm. We recovered 840 unique structure factors for several different thicknesses and beam energies. Structure factors for electron diffraction were obtained from Ref. [4] with a mean absorption included on the diagonal of A. The only effect of this potential is a constant rescaling of the S matrix magnitudes, which are renormalized at the start of the reconstruction algorithm. The entry in the center of A was the direct beam. In general there are $(N^2-1)/2$ free real parameters in Hermitian A when account is taken of the antidiagonal symmetry. This is reduced further here by crystal symmetry to $2(N-\sqrt{N})$.

Each reconstruction ran for a total of 200 iterations. In the cases where step (10) was used, we alternated between 50 iterations of charge flipping followed by 50 iterations of charge flattening, repeated twice. All reconstructions took less than 10 min on a desktop machine. In step (10), the tolerance τ was set at each iteration to be above 90% of the potential values computed in step (9). During flipping we used $\alpha = -1/2$ instead of the traditional -1 to dampen oscillations in the solvent regions leading to improved convergence.

In order to asses the quality of the reconstructions, we aligned each to the ground truth and computed a Pearson correlation coefficient between the two resulting potentials, which are listed in Tables I and II and Table S1 in Ref. [18]. Surface plots of the ground truth and reconstructed potentials are shown in Fig. 1 and in Figs. S7–S14 in Supplemental Material [18]. Computing λ from A is shown to be superior for smaller thicknesses, while computing λ from M is better at larger thicknesses. This is due to the fact that at smaller thicknesses, the eigenvalues of A provide extra constraints on the eigenvalues of S, but, as discussed earlier, this relationship becomes unstable for large t. Computing λ from M avoids this instability since the eigenvalues of A are not used at all in the computation of S.

Table II shows that for sufficiently large thickness, flipping is not needed, and, therefore, multiple scattering contains sufficient information to solve the phase problem directly without the need for additional real-space constraints, such as support or atomicity (atomic-resolution data). For spinel, with 71 atoms in the cubic cell, charge flipping was found to be less effective, as its 2D projected potential is much denser than GaAs, but reconstruction was still possible for sufficiently thick crystals due to the extra information provided by multiple scattering.

Additional results are provided in the Supplemental Material [18]. Table SI and Fig. S11 demonstrate that a precise estimate of thickness is not needed in the λ from A version, as t can be found during the reconstruction without a significant change in the quality of the reconstruction. Figure S14 shows that reconstruction is still possible when

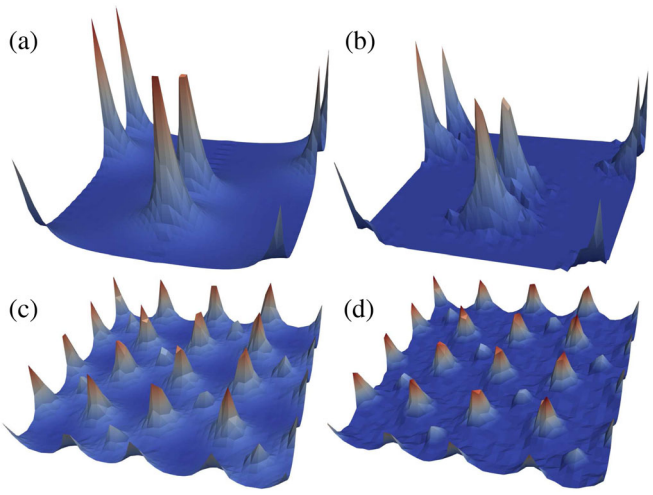

FIG. 1. GaAs (a),(b) and spinel (c),(d) potential maps projected along [110] and [100], respectively. (a),(c) Ground truth. (b),(d) Recovered from Bragg intensities extending to less than 1 Å resolution with $N = 441$, for a beam energy of 300 kV in the zone axis orientation at a thickness of 100 nm by computing λ from M with (b) and without (d) flipping.

several columns of M are not available and how reconstruction quality is affected by missing columns.

The algorithms starts to fail at very high energies (see 1000 kV). Then the Ewald sphere becomes very flat, causing diagonal entries of A to approach 0. The linear system relating the branch cuts to the diagonals of A then becomes homogeneous, and is solved by any scalar multiple of the true branch cuts and the trivial solution $x = 0$ corresponding to the principal branch cut. For small thickness this does not present a problem, as the principal branch cut is then the correct branch cut for each eigenvalue.

Applications of the method to experimental data will require elastically filtered diffraction patterns [25]. For the application of the method to soft x-ray scattering [26,27], where charge density plays the role of potential, the main limitation will be the neglect of backscattering and beam polarization effects. Reference [28] describes a way to include 3D effects of structure factors not lying in a plane normal to the beam (but near the Ewald sphere), while Refs. [29,30] include backscattering, both retaining our formalism. These 3D higher-order laue zones (HOLZ) structure factors, describing variation of the potential $V(\mathbf{r})$ along the beam direction, might then be recovered. For the larger unit-cell protein crystals studied by Micro-electron diffraction where HOLZ Bragg spots may appear at high tilts, the Ref. [18] provides a relationship between periodicity along the beam direction c and resolution d if limited to the range within which HOLZ reflections do not appear. We find $d = 0.25$ nm for $c = 16$ nm at 200 kV.

With further development, an adapted algorithm could reduce R factors in protein crystallography for low-order reflections in high-quality crystals, revealing new features in charge-density maps affected by multiple scattering. For diffractive x-ray imaging, where denser Shannon, rather than Bragg sampling is needed, the algorithm might provide a general method of lensless imaging. Application of the method to the removal of multiple scattering from Cryo-electron microscopy images remains to be investigated.

This work was funded by the Advanced Scientific Computing Research and Basic Energy Sciences programs of the Office of Science of Department of Energy (DOE) (Award No. DE-AC02-05CH11231), by Laboratory Directed Research and Development funds from Berkeley Lab from the Director, Office of Science DOE (Award No. DE-AC02-05CH11231), and by NSF BioXFEL STC Grant No. 1231306.

[1] Q. Shen, Phys. Rev. Lett. **80**, 3268 (1998).
[2] H. Bethe, Ann. Phys. (Berlin) **392**, 55 (1928).
[3] P. Goodman and A. Moodie, Acta Crystallogr. Sect. A **30**, 280 (1974).
[4] J. M. Zuo and J. C. H. Spence, *Advanced Transmission Electron Microscopy* (Springer, New York, 2017).
[5] A. F. Moodie, Z. Naturforsch. **27a**, 437 (1972).
[6] C. Koch and J. Spence, J. Phys. A **36**, 803 (2003).
[7] F. Wang, R. S. Pennington, and C. T. Koch, Phys. Rev. Lett. **117**, 015501 (2016).
[8] J. C. H. Spence, Acta Crystallogr. Sect. A **54**, 7 (1998).
[9] A. M. Maiden, M. J. Humphry, and J. M. Rodenburg, J. Opt. Soc. Am. A **29**, 1606 (2012).
[10] J. C. H. Spence, B. Calef, and J. M. Zuo, Acta Crystallogr. Sect. A **55**, 112 (1999).
[11] P. Rez, Acta Crystallogr. Sect. A **55**, 160 (1999).
[12] J. C. H. Spence, Acta Crystallogr. Sect. A **65**, 28 (2009).
[13] L. J. Allen, T. W. Josefsson, and H. Leeb, Acta Crystallogr. Sect. A **54**, 388 (1998).
[14] H. G. Brown, Z. Chen, M. Weyland, C. Ophus, J. Ciston, L. J. Allen, and S. D. Findlay, Phys. Rev. Lett. **121**, 266102 (2018).
[15] L. Sturkey, Proc. Phys. Soc. **80**, 321 (1962).
[16] A. J. F. Metherell, in *Electron Microscopy in Materials Science*, edited by U. Valdre and E. Ruedl (Commission of European Communities, Brussels, 1975), p. 401.
[17] M. Kogiso and H. Takahashi, J. Phys. Soc. Jpn. **42**, 223 (1977).
[18] See Supplemental Material at http://link.aps.org/supplemental/10.1103/PhysRevLett.125.065502 for flow-charts, more results, simulations with fewer diffraction patterns and HOLZ effects.
[19] L. J. Allen, H. Leeb, and A. E. C. Spargo, Acta Crystallogr. Sect. A **55**, 105 (1999).
[20] G. Auberson, A. Martin, and G. Mennessier, Commun. Math. Phys. **140**, 523 (1991).
[21] L. M. Bregman, USSR Computational Mathematics and Mathematical Physics **7**, 200 (1967).
[22] J. McKeown and J. Spence, J. Appl. Phys. **106**, 074309 (2009).
[23] G. Ozlanyi and A. Suto, Acta Crystallogr. Sect. A **60**, 134 (2004).
[24] Although the transform in step (6) does not yield the closest unitary matrix to $\tilde{S}^n$, we found this choice to provide more stability in the reconstruction algorithm.
[25] J. M. Zuo, M. Kim, M. O'Keeffe, and J. C. H. Spence, Nature (London) **401**, 49 (1999).
[26] D. Shapiro, P. Thibault, T. Beetz, V. Elser, M. Howells, C. Jacobsen, J. Kirz, E. Lima, H. Miao, A. M. Neiman, and D. Sayre, Proc. Natl. Acad. Sci. U.S.A. **102**, 15343 (2005).
[27] A. Hare and G. Morrison, J. Mod. Opt. **41**, 31 (1994).
[28] A. L. Lewis, R. E. Villagrana, and A. J. F. Metherell, Acta Crystallogr. Sect. A **34**, 138 (1978).
[29] D. Lynch and A. Moodie, Surf. Sci. **32**, 422 (1972).
[30] J. H. Chen and D. Van Dyck, Ultramicroscopy **70**, 29 (1997).